Chemical Science

ROYAL SOCIETY OF CHEMISTRY

EDGE ARTICLE

View Article Online
View Journal



Cite this: DOI: 10.1039/d6sc02906j

All publication charges for this article have been paid for by the Royal Society of Chemistry

# A nickel/cobalt-free Mn-based layered oxide cathode based on an orbital hybridization modulation strategy for high energy density sodium-ion batteries

Zhuozheng Hong,†[ab] Xin-Yu Zhang,†[b] Minwen Yang,†[c] Yan-Fang Zhu,[b] Diancheng Chen,[c] Yan-Jiang Li,[d] Haojie Dong,[e] Yaping Yan,*[h] Yubin Niu,[f] Peng-Fei Wang,[e] Yang Sun,*[c] Chao Wu*[a] and Yao Xiao*[bg]

Conventional nickel–manganese-based layered oxides, due to their high energy density, are promising cathode materials for sodium-ion batteries (SIBs). However, the relatively high cost of elements such as nickel and cobalt poses a challenge to the development of cost-effective SIBs for large-scale energy storage. To address this issue, we designed a Co/Ni-free cathode *via* a rational orbital hybridization modulation strategy, in which Mg is selected as the modulator to replace Ni. The substitution of nickel with magnesium not only reduces material cost but also, more importantly, enables magnesium to act as an electronic structure regulator. Guided by this design principle, combined theoretical and experimental analyses reveal that $Mg^{2+}$ eliminates the strong and unstable hybridization present in the counterpart material $Na_{0.55}Ni_{0.1}Fe_{0.1}Mn_{0.8}O_2$ (NFM118). This effect broadens and improves the O 2p band, thereby lowering the energy barrier for electron transfer between Mn 3d and O 2p orbitals. This unique charge compensation mechanism, effectively suppresses the Jahn–Teller distortion and irreversible oxygen evolution. Consequently, the MFM118 cathode delivers a high reversible capacity of 180.78 mAh $g^{-1}$ within 1.5–4.3 V and exhibits superior rate performance and significantly enhanced cycling stability. This work highlights the advantage of orbital hybridization modulation in developing cost-effective and high-performance SIB cathodes.

Received 8th April 2026
Accepted 1st May 2026

DOI: 10.1039/d6sc02906j

rsc.li/chemical-science



## Introduction

Sodium-ion batteries (SIBs) have emerged as a compelling complementary technology to lithium-ion batteries (LIBs) for large-scale energy storage, primarily driven by the natural abundance, even geographical distribution, and low cost of sodium resources.[1–9] The commercial viability and sustainable development of SIBs, however, critically depend on cathode materials that simultaneously deliver high energy density, long cycle life, and low cost.[10–16] Among various candidates, layered transition metal (TM) oxides, $Na_xTMO_2$, are particularly attractive owing to their high theoretical capacity and relatively simple synthesis. These materials are typically classified into P2- and O3-types based on the coordination geometry of sodium ions (prismatic or octahedral) and the stacking sequence of TM-oxygen layers.[17–21] The P2-type structure, with larger interlayer spacing, often demonstrates superior ionic conductivity and rate performance.[22–24]

Nonetheless, the practical application of these materials faces a dual, intertwined challenge. First, the ever-growing demand for costly and scarce nickel (and cobalt) poses a significant economic hurdle for cost-effective, large-scale application.[25–27] Second, and more fundamentally, the electrochemical instability stemming from structural degradation and irreversible oxygen redox at high voltages severely limits their cycle life.[5] Simply reducing nickel content to address the cost issue often exacerbates the stability problem, as the remaining TM framework becomes more susceptible to detrimental phase

[a]*Institute of Energy Materials Science (IEMS), University of Shanghai for Science and Technology, Shanghai, 200093, P. R. China. E-mail: chaowu@usst.edu.cn*

[b]*College of Chemistry and Materials Engineering, Wenzhou University, Wenzhou, 325035, P. R. China. E-mail: xiaoyao@wzu.edu.cn*

[c]*School of Materials, Sun Yat-sen University, Shenzhen 518107, China. E-mail: sunyang5@mail.sysu.edu.cn*

[d]*Key Laboratory of Spin Electron and Nanomaterials of Anhui Higher Education Institutes, Suzhou University, Suzhou 234000, China*

[e]*Center of Nanomaterials for Renewable Energy, State Key Laboratory of Electrical Insulation and Power Equipment, School of Electrical Engineering, Xi'an Jiaotong University, Xi'an, Shaanxi 710049, P. R. China*

[f]*School of Materials and Energy, Southwest University, Chongqing, 400715, P. R. China*

[g]*State Key Laboratory of Critical Metals Beneficiation, Metallurgy and Purification, Zhengzhou University, Zhengzhou, Henan, 450002, P. R. China*

[h]*Henan Engineering Technology Research Center for Fiber Preparation and Modification, Henan International Joint Laboratory of Rare Earth Composite Materials, Henan University of Engineering, Zhengzhou, Henan, 451191, P. R. China. E-mail: yyp1990@haue.edu.cn*

† Zhuozheng Hong, Xin-Yu Zhang and Minwen Yang contributed equally to this work.

transitions and irreversible anionic redox, resulting in oxygen release, TM dissolution, and rapid capacity fade.[28–30] Therefore, developing high-performance cathodes completely free of costly cobalt and nickel, without compromising structural and interfacial stability, is a paramount yet unmet goal for SIBs. Conventional modification strategies, such as elemental doping or surface coating, often provide incremental improvements but fail to address the root cause of the instability—the electronic structure and the associated charge compensation mechanism at high voltages.[31–36] These strategies typically focus on the ionic radius or charge balance, without directly engineering the orbital-level interactions that govern redox activity and structural evolution.[37,38]

Herein, we propose and demonstrate a strategy rooted in orbital hybridization modulation to fundamentally overcome the above limitations. Instead of a mere elemental substitution for cost reduction, we rationally engineer the local electronic structure. We designed a low-cost, cobalt/nickel-free cathode, $Na_{0.55}Mg_{0.1}Fe_{0.1}Mn_{0.8}O_2$ (MFM118), by deliberately substituting nickel with electrochemically inert magnesium.[39–44] Specifically, spectroscopic analyses and structural refinements confirm that Mg substitution effectively suppresses Jahn–Teller distortion by elevating the average Mn valence state. More importantly, this substitution reconstructs the charge compensation, as directly evidenced by *ex situ* X-ray absorption spectroscopy, which captures an anomalous reduction of Mn during high-voltage charging. *In situ* XRD reveals that this electronic regulation translates into exceptional structural stability, manifested as a P2/OP4 phase coexistence which alleviates strain. At the interface, electrochemical impedance spectroscopy (EIS) combined with distribution of relaxation times (DRT) analysis, alongside time-of-flight secondary ion mass spectrometry (TOF-SIMS) and transmission electron microscopy (TEM), demonstrates that Mg substitution drastically suppresses TM migration and promotes the formation of a thin, uniform cathode–electrolyte interphase, leading to superior interfacial kinetics and stability. Consequently, this integrated stabilization from the atomic to the micron scale culminates in outstanding electrochemical performance, with MFM118 delivering a high reversible capacity of 180.78 mAh $g^{-1}$, remarkable rate capability, and enhanced cycling stability. The advantage of this work lies in elucidating how orbital hybridization engineering unlocks a stable and efficient charge compensation mechanism, laying the foundation for developing green, low-cost, and high-energy-density cathode materials.

## Results and discussion

In this work, NFM118 was successfully prepared by the solid-state method, and the pure phase MFM118 was obtained by replacing Ni with Mg. The Rietveld refinement of XRD patterns confirms that both NFM118 and MFM118 crystallize in a P2-type layered structure with the $P6_3/mmc$ space group (Fig. 1a and b). A critical observation is the reduction of the *c*-axis lattice parameter from 5.6437 Å in NFM118 to 5.6315 Å in MFM118. This contraction is a primary indicator of suppressed Jahn–Teller distortion and enhanced electrostatic shielding between adjacent oxygen layers induced by the higher charge density of $Mg^{2+}$, which reduces O–O repulsion and more than compensates for the minor difference in ionic radii. Electron paramagnetic resonance (EPR) spectra reveal distinct electronic states (Fig. 1c). MFM118 exhibits a signal at $g \approx 2.0389$, characteristic of stabilized hole states on oxygen (*e.g.* peroxo-like species, $(O_2)^{n-}$) and the presence of Jahn–Teller-inactive $Mn^{4+}$ ions. In stark contrast, NFM118 shows a broad signal at $g \approx 2.3363$, a signature of strong Jahn–Teller activity associated with $Mn^{3+}$ and $Ni^{3+}$ ions, which cause significant local lattice distortion and electron localization. This interpretation is corroborated by X-ray photoelectron spectroscopy (XPS) and X-ray absorption near-edge structure (XANES) spectra at the Mn K-edge (Fig. 1d, e and S3).[45] The average Mn oxidation state in NFM118 is approximately +3.5, indicating a substantial population of Jahn–Teller active $Mn^{3+}$ ions, while in MFM118, the average Mn oxidation state is calculated to be approximately +3.7, which is significantly elevated relative to NFM118 and corresponds to a markedly reduced proportion of Jahn–Teller-active $Mn^{3+}$, consistent with a dominantly Jahn–Teller inactive electronic configuration. The Ni K-edge XANES confirms that Ni remains in the +2 oxidation state in NFM118. Collectively, these data demonstrate that Mg substitution effectively suppresses the Jahn–Teller effect by elevating the average Mn valence and eliminating $Ni^{3+}$, thereby creating a more stable local electronic environment. This stabilized local electronic environment suggests a modification in the fundamental charge compensation pathway, which will be discussed later.[46] Scanning electron

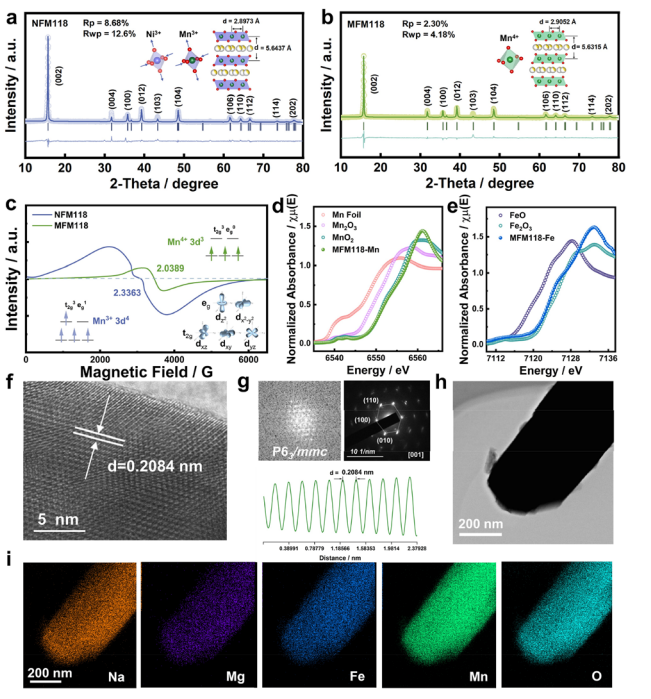


Fig. 1 Structural characterization from macroscopic to atomic scales. (a and b) XRD Rietveld refinement results for NFM118 and MFM118. (c) *Ex situ* EPR spectra of NFM118 and MFM118. (d and e) Normalized Mn K-edge XANES and Fe K-edge XANES spectra of MFM118. (f) HR-TEM images of MFM118. (g) FFT modes and intensity line profile of MFM118. (h and i) TEM-EDS element distribution mapping of MFM118.

microscopy (SEM) and TEM characterization showed that both samples exhibit a similar irregular brick-like morphology with particle sizes ranging from 6 to 8 micrometers (Fig. S4). High-resolution transmission electron microscopy (HRTEM), fast Fourier transform (FFT), and selected area electron diffraction (SAED) images revealed that the *d*-value spacing of MFM118 was 2.084 Å, which was consistent with the (103) crystal plane spacing of the P2 phase, and the *d*-value spacing of NFM118 was 5.64 Å, which was in agreement with the (002) crystal plane spacing of the P2 phase. This confirmed the P2-type structure of both materials (Fig. 1f, g, S5 and 6).[47] Finally, high-angle annular dark-field scanning TEM combined with energy-dispersive X-ray spectroscopy (EDS) mapping confirmed the uniform distribution of all elements in both cathode materials, indicating successful Mg incorporation without secondary phase formation (Fig. 1h, i and S7).

### Electrochemical performance and kinetics behavior

The charge–discharge curves and cyclic voltammetry (CV) curves reveal the fundamental differences in the electrochemical behavior of these two materials (Fig. 2a–d). This indicates a complex and interrelated redox process involving $Ni^{2+}/Ni^{4+}$ and irreversible lattice oxygen oxidation, which leads to structural rearrangement. In contrast, MFM118, where the electrochemically inert $Mg^{2+}$ is present, shows a lower initial capacity (about 90 mAh $g^{-1}$), but its charging curve is very smooth. The reduced initial charge capacity of MFM118 compared to NFM118 is attributed to both the elimination of Ni redox contribution (due to the electrochemically inert nature of $Mg^{2+}$) and a brief kinetic activation process required for the newly configured O 2p band to fully engage in reversible anionic redox, after which the material delivers stable high capacity. Its CV curve presents a single and sharp oxidation peak above 4.0 V, which is a signature of the highly reversible anionic redox process enabled by our orbital hybridization modulation. Meanwhile, the more distinct redox peaks in the low-voltage range of the CV curve are believed to be caused by the valence state change of Mn. This is the first electrochemical feature of the reconstructed charge compensation. This reconstruction mechanism directly translates into superior electrochemical kinetics and stability. MFM118 exhibits exceptional rate capability (Fig. 2e), significantly outperforming NFM118 at high current densities. This is attributed to the stable framework and reversible surface reactions minimizing impedance growth. This can also be seen in the specific energy at different rates in Fig. S8, where MFM118 shows superior rate performance. Meanwhile, the comparison of the charge–discharge curves of the two materials at different rates as shown in Fig. 2f, g and S9 indicates that MFM118 has a smaller capacity and energy decay at high rates compared to NFM118, further verifying that the substitution of Mg can greatly improve stability.

Considering the excellent rate performance of MFM118, CV and galvanostatic intermittent titration technique (GITT) tests were conducted at different scan rates to quantitatively

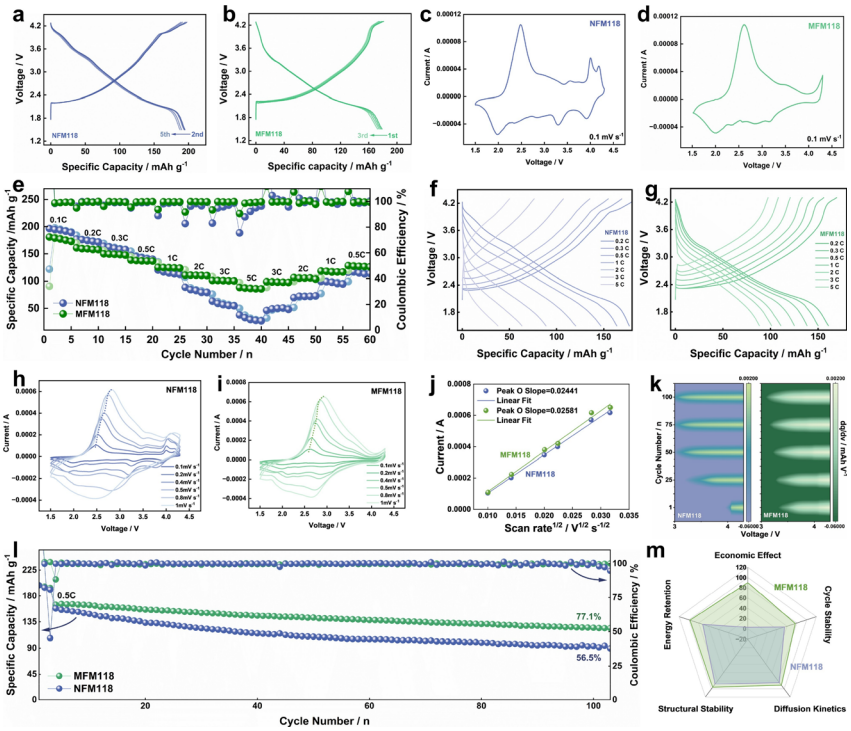


Fig. 2 The electrochemical performance of NFM118 and MFM118. (a and b) Charge–discharge curves for the second to fifth cycles at 0.1C. (c and d) First-cycle CV curves at 0.1 mV $s^{-1}$. (e) Rate performance from 0.1 to 5C. (f and g) Charge–discharge profile from 0.2 to 5C. (h and i) CV curves from 0.1 mV $s^{-1}$ to 1 mV $s^{-1}$. (j) Linear fit of the peak current of the O2 peak to the square root of the scan rate. (k) The d*Q*/d*V* contour plots of voltage capacity charge with different from 3 to 4.3 V. (l) Cycling performance over 100 cycles at 0.2C within the voltage range of 1.5–4.3 V after rate performance tests. (m) Electrochemical comprehensive performance radar comparison chart.

determine the $Na^+$ diffusion coefficient of MFM118, as shown in Fig. 2h–j and Tables 1 and 2. Compared with NFM118, MFM118 exhibited a higher current response with distinct redox peaks. The diffusion coefficient was quantitatively calculated by fitting the linear relationship between the peak current ($I_p$) and the square root of the scan rate ($v^{1/2}$) (Fig. 2j). According to the Randles–Sevcik equation, MFM118 demonstrated a stable apparent $Na^+$ diffusion coefficient, indicating a faster kinetic behavior. To better understand the diffusion of sodium ions during the charge and discharge process, GITT measurements were used to calculate the diffusion coefficient. Throughout the process, MFM118 exhibited a superior $Na^+$ diffusion coefficient (Fig. S10 and 11). This is attributed to the more stable crystal structure constructed by Mg substitution, which not only suppresses irreversible phase transitions that could block diffusion pathways but also facilitates a more reversible surface reaction, leading to a thinner and more uniform cathode–electrolyte interphase (CEI). This combination significantly enhances the pseudocapacitive contribution and the sodium ion diffusion rate. Consequently, the material achieves faster charge storage at high scan rates, thereby demonstrating its superior rate performance and fast charge–discharge capability. To facilitate the comparison of the trends in electrochemical performance, the peaks of the d$Q$/d$V$ curves at different cycles were analyzed through line graphs and corresponding contour plots (as shown in Fig. 2k, S12 and 13). After multiple cycles, the peaks all showed regular changes. From the first cycle to the 100th cycle, the characteristic peaks of MFM118 shifted slightly during repeated charge and discharge processes. However, the characteristic peaks of NFM118 gradually showed non-vertical shifts. This potential shift is related to the overpotential shift caused by battery polarization. This polarization may be related to the inherent loss of active sodium ions. At the same time, the analysis of the d$Q$/d$V$ curves from the 1st to the 20th cycle shows that the curves of MFM118 are highly overlapping, indicating that the substitution of Mg can reduce the impact of battery polarization. In addition, a long cycle experiment at 0.2C between 1.5 and 4.3 V was conducted to examine the high-rate stability of capacity and structure. As shown in Fig. 2i, MFM118 retained 77.1% of its capacity after 100 cycles, significantly higher than the 56.5% of NFM118. This indicates that MFM118 has a higher capacity and better cycling stability, further verifying the inhibitory effect of Mg substitution on phase transformation and ion migration in the material. Meanwhile, to more intuitively compare the comprehensive electrochemical performance of MFM118 and NFM118, a radar comparison chart was made (Fig. 2m). The research results once again confirmed the significance of Mg in enhancing the performance of SIBs, as MFM118 exhibited the best overall electrochemical performance.[48]

### Dynamic structural evolution

To precisely track the structural evolution of the MFM118 cathode material during sodium ion (de)insertion, *in situ* XRD measurements were conducted at a current density of 0.2C (Fig. 3a, b and S14). For MFM118, the original P2 phase shifted slightly towards a lower angle at low voltages (the (002) peak), indicating a *c*-axis expansion due to $Na^+$ extraction. At high voltages, the intensity of the P2 peak decreased, while a new diffraction peak emerged at a $2\theta$ value of approximately 16.1°, confirming the formation of an OP4 phase. During the discharge process, this mixed phase reverted to the P2 phase, defining the phase transformation path of MFM118 as P2 → P2/OP4 → P2. The persistence of the main P2 peak suggests that the phase transformation requires overcoming an energy barrier, which may not be fully surmounted within the limited charging/discharging time.[49] This results in a partially transformed structure where some regions transition to the OP4 phase, while others remain metastable in the P2 configuration due to local energy barriers or $Na^+$ concentration gradients, leading to a coexistence of the two phases. $Mg^{2+}$, acting as an inert and robust locking ion randomly distributed in the TM layer, locally anchors the surrounding crystal structure, effectively inhibiting slab gliding and phase transformation. Consequently, in regions with a high concentration of $Mg^{2+}$, the structure is pinned and remains in the P2 phase, whereas in regions with low or no $Mg^{2+}$, the structure is more prone to slip and transform into the OP4 phase. According to FAULTS simulations (Fig. 3c–e and S15), the intensity of the main P2 peak decreases but remains observable, strongly indicating a widespread coexistence of P2 and OP4 phases within the bulk material. This represents a non-equilibrium state governed by both kinetics and thermodynamics. During charging, as $Na^+$ is continuously extracted beyond the stability limit of the P2 phase, the transformation begins. However, the random distribution of $Mg^{2+}$ and its locking effect prevent a uniform transformation, leading to a mosaic-like nano-domain structure within the material: some areas transform into the OP4 phase, while regions stabilized by $Mg^{2+}$ tenaciously retain the P2 phase. This nano-scale phase coexistence alleviates the immense internal strain associated with a complete single-phase transformation, thereby enhancing the structural reversibility and cycling stability.

### Interface stability mechanism

To investigate the electrochemical processes at the electrode–electrolyte interface after cycling, *in situ* and *ex situ* EIS were performed on the half-cells (Fig. 4a–d and S16). It was found that during charging up to 4.3 V, the second semicircle (associated with the interface resistance, $R_{ct}/R_{film}$) of MFM118 was smaller and remained relatively stable compared to that of NFM118, showing only a brief increase near 4 V, potentially related to the onset of the reversible oxygen redox reaction. A consistent trend was observed during discharge, indicating that Mg substitution improves the interfacial kinetics. This result was further verified by *ex situ* EIS. To gain deeper insight into the interfacial kinetics, the DRT was analyzed from the impedance data (Fig. 4e–h and S17).[50,51] The T1 peak, which is typically associated with charge transfer and interfacial processes at the electrode surface, exhibited a smaller width and a decreasing intensity during both charging and discharging for MFM118 compared to NFM118. The smaller peak

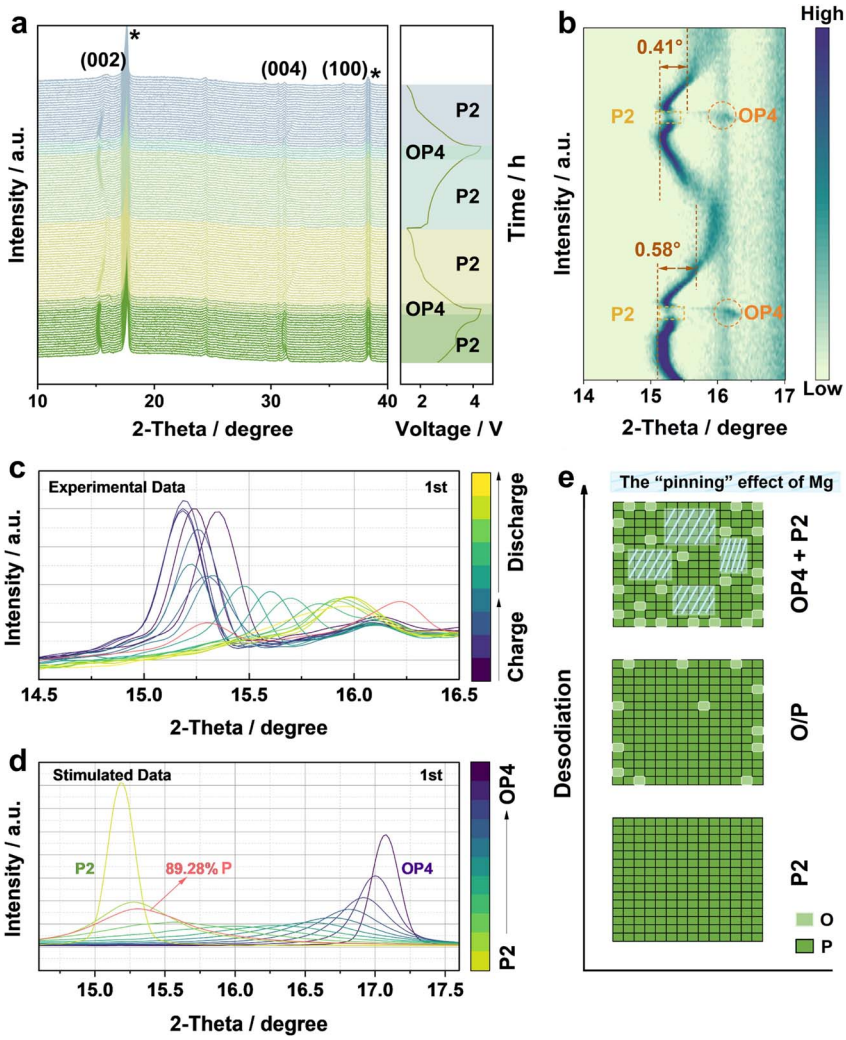


Fig. 3 Crystal structural evolution of MFM118 during $Na^+$ extraction/insertion. (a) *In situ* XRD patterns collected during the charge/discharge in the voltage range of 1.5–4.3 V. (b) The 3D counter graphs of the main characteristic diffraction peaks. (c) *In situ* XRD patterns for the P2 to OP4 phase evolution. (d) FAULTS simulations of the P2/OP4 intergrowth phase. (e) Proportion of P2 and OP4 phase stacks in the MFM118 electrode during the desodiation process.

width suggests a more homogeneous time constant distribution, indicative of a more uniform and stable interface. The decrease in peak intensity as the reaction progresses implies a reduction in the resistance associated with that specific process. In contrast, the $T = 1$ peak for NFM118 showed broader distribution and less regular changes, suggesting more heterogeneous and irreversible interfacial reactions, likely due to severe side reactions like irreversible oxygen oxidation and TM dissolution. This DRT analysis is consistent with the EIS results, demonstrating that Mg substitution leads to significantly improved interfacial kinetics and stability, which is a direct consequence of the more reversible charge compensation mechanism and the suppression of detrimental side reactions.

After subjecting the NFM118 and MFM118 half-cells to 200 cycles, the cells were disassembled for TOF-SIMS characterization of the electrodes (Fig. 4i–m). For NFM118, the intensity of the $MnF_3^-$ signal decreased uniformly from the interface towards the bulk phase, indicating that the Mn undergoes severe migration and dissolution during the cycling process.[52] In contrast, the interface intensities of $MnF_3^-$, $MgF_3^-$, and $FeF_2^-$ signals were very low in MFM118, verifying that Mg substitution effectively suppresses TM migration. Furthermore, the intensity of the $NaF_2^-$ signal remained almost unchanged in MFM118, suggesting a more uniform distribution of the CEI, whereas its intensity varied significantly in NFM118, indicating an uneven CEI layer. This difference is further corroborated by the less uniform distribution of $C_2HO^-$ fragments in NFM118 compared to MFM118 (Fig. S18 and 19). The uniformity of the distribution of this group is related to the decomposition products of the electrolyte. Its uneven distribution will affect the uniformity of the CEI layer. TEM imaging of the cycled electrodes (Fig. S20 and 21) visually confirmed these findings: the CEI layer of NFM118 was thick and uneven (up to ~305 nm in some areas), while the CEI layer on MFM118 was uniformly thin (~9 nm). This indicates that Mg doping effectively suppresses

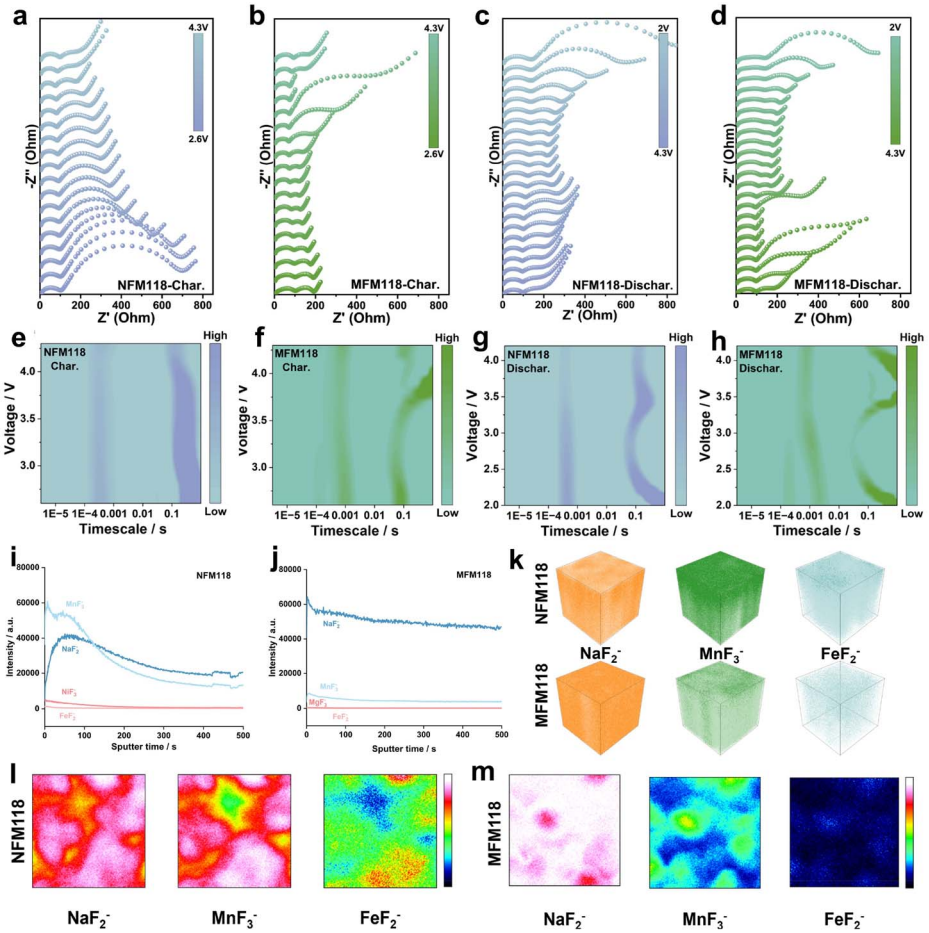


Fig. 4 Interface variation capability evaluation. (a–d) *In situ* EIS plots of the NFM118 and MFM118 electrodes at 1.5–4.3 V. (e–h) DRT analysis based on impedance spectra. (b) The 3D counter graphs of the main characteristic diffraction peaks. (i and j) Normalized TOF-SIMS depth profiles. (k–m) Overlapping 3D and 2D renderings of TOF-SIMS fragments for NFM118 and MFM118 electrode surfaces after cycling.

the side reactions between the electrode and the electrolyte, which is conducive to the ordered migration of sodium ions.

### Charge compensation mechanism

The charge compensation mechanisms in NFM118 and MFM118 were probed using *ex situ* X-ray absorption spectroscopy (XAS) (Fig. 5a and b). When charged to 4.0 V, the manganese valence state in NFM118 changes only slightly from its pristine state (~+3.5), indicating minimal participation of Mn in redox reactions within this voltage window. However, upon charging to 4.3 V, the Mn valence shifts towards higher energy, signifying the oxidation of remaining $Mn^{3+}$ to $Mn^{4+}$, which contributes to the capacity above 4.0 V alongside Ni and oxygen oxidation. In stark contrast, the Mn valence in MFM118 moves towards a lower energy direction when charged to 4.3 V compared to its state at 4.0 V, clearly indicating a charge redistribution process where electron density is back from the stabilized O 2p orbitals to the Mn 3d orbitals.[53] This phenomenon of not rising but falling at high voltage is not simply the reduction of manganese, but rather the result of internal charge rearrangement of the entire material system under the regulation of $Mg^{2+}$ substitution, enabling efficient and reversible anionic redox. Compared with NFM118, when charged to 4.3 V, its Mn K-edge shifts towards higher energy, which is a typical sign of the oxidation of $Mn^{3+}$ to $Mn^{4+}$. The oxygen oxidation behavior couples with the strong oxidizability of Ni, leading to irreversible oxidation of oxygen, the formation of oxygen vacancies and the release of oxygen. However, the Mg substitution in MFM118 realizes a reversible oxygen-coupled charge compensation mechanism. Oxygen is reversibly oxidized and reduced, during which electrons transfer from the 3d orbitals of $Mn^{4+}$ to the 2p orbitals of O, thus avoiding irreversible oxygen loss. This phenomenon of not rising but falling at high voltage is not simply the reduction of manganese, but the result of internal charge rearrangement of the entire material system under the regulation of $Mg^{2+}$ substitution to achieve efficient and reversible anion redox. The reduction of Mn is the key evidence and component of this stable and reversible oxygen redox mechanism. Analysis of the EXAFS spectra in *R*-space (Fig. 5c–e) reveals that the Mn–O bond length in MFM118 has a tendency to lengthen during charging, which confirms the reduction of Mn. The ionic radius of $Mn^{3+}$ (0.645 Å, high-spin) is higher than that of $Mn^{4+}$ (0.53 Å), leading to a longer average Mn–O bond.[54] Concurrently, $Mn^{3+}$ is a Jahn–Teller ion, causing further octahedral distortion and elongation, which also

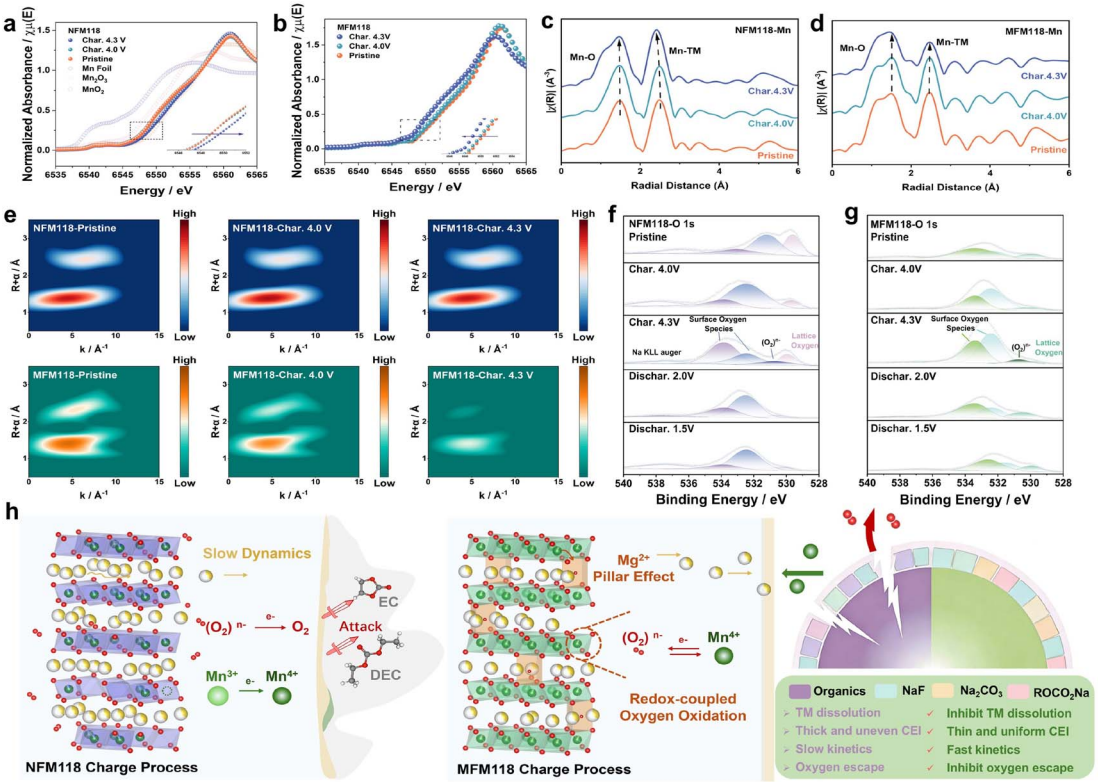


Fig. 5 Mechanism and evaluation of the Mg substitution effect. (a and b) Mn K-edge XANES of NFM118 and MFM118 at various charging states. (c and d) EXAFS spectra of NFM118 and MFM118 at various charging states. (e) WT-EXAFS spectra of the Mn K-edge for NFM118 and MFM118 at various charging states. (f and g) O 1s *ex situ* XPS spectra for NFM118 and MFM118. (h) Schematic diagram of the Mg pillar effect inhibiting the lattice oxygen escape mechanism.

increases the bond length. The formation of O–O bonds or oxygen vacancies upon oxygen oxidation can also contribute to an increase in the average Mn–O bond length.[55]

Wavelet transform analysis of the EXAFS data shows that the intensity of the Mn–O and Mn–TM coordination peaks weakens significantly at higher voltages, indicating increased local structural disorder and bond length distribution, likely associated with Jahn–Teller distortion.

*Ex situ* XPS analysis of the O 1s region (Fig. 5f, g and S22–24) provides further evidence. When NFM118 is charged to 4.3 V, the lattice oxygen peak shifts to higher binding energy and its intensity decreases, directly proving oxygen oxidation and the formation of oxygen vacancies. Upon discharge to 1.5 V, the lattice oxygen signal remains abnormally weak, indicating that the oxygen released during high-voltage charging cannot be reversibly reincorporated into the lattice, resulting in permanent oxygen loss and surface degradation.[56] In stark contrast, for MFM118, the lattice oxygen peak shifts towards lower binding energy upon discharge and its intensity recovers almost completely to that of its pristine state, thereby unequivocally demonstrating a highly reversible oxygen redox reaction. Fig. 5h schematically illustrates this contrasting behavior: MFM118 follows a reversible, oxygen-coupled charge compensation mechanism enabled by Mg substitution, achieving excellent cycle stability. In contrast, NFM118 undergoes an irreversible cation–oxygen coupled oxidation path, leading to structural degradation and capacity fade.

## Theoretical calculations

To unravel the fundamental mechanism by which Mg substitution reconstructs charge compensation, we conducted comprehensive density functional theory (DFT) calculations. The analysis of the Electron Localization Function (ELF) provides the first crucial insight (Fig. 6a–d).[57] For NFM118, significant electron localization is observed along the Ni–O bonds, indicative of strong covalent character and substantial Ni 3d–O 2p orbital hybridization. This strong hybridization elevates the energy of the localized O 2p states near the Fermi level, rendering them highly reactive and prone to irreversible oxidation and oxygen loss at high voltages, which aligns with the observed severe structural degradation. In stark contrast, MFM118 exhibits ionic character in the Mg–O bonds, with electrons localized around oxygen anions. The absence of such strong covalent hybridization with the electrochemically inert $Mg^{2+}$ prevents the formation of those unstable, high-energy O 2p states.[58]

The projected density of states (pDOS) analysis offers deeper electronic structure insights (Fig. 6i and j). For NFM118, the Ni 3d band strongly hybridizes with the O 2p band, creating a continuous electronic state across the Fermi level. While this indicates metallic conductivity, the hybridized O 2p states are highly localized and energetically raised, making them susceptible to irreversible oxidation.[59,60] Crucially, in MFM118, the substitution of Ni with Mg eliminates this strong covalent hybridization center. The ionic field of $Mg^{2+}$ induces an upward

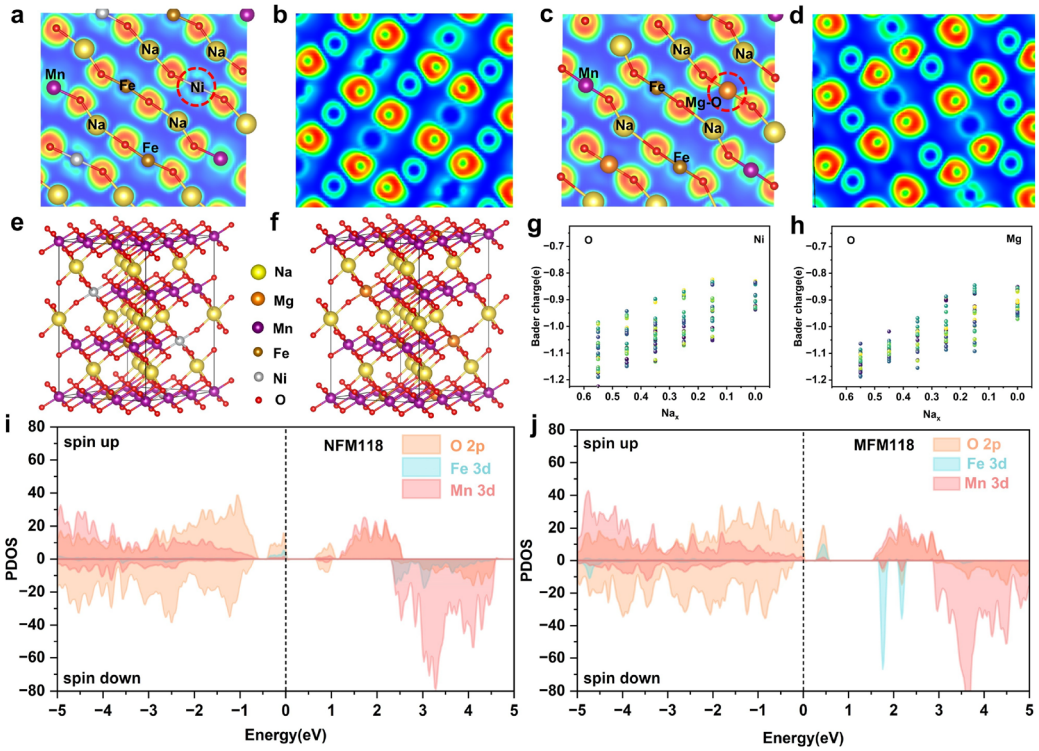


Fig. 6 DFT calculations of TMFM118 samples. (a–d) Theoretical calculations of ELF for NFM118 and MFM118. (e and f) The structural configuration of $Na_{15}Ni_3Fe_3Mn_{21}O_{54}$ and $Na_{15}Mg_3Fe_3Mn_{21}O_{54}$. (g and h) The Bader charge calculation results of two O configurations. (i and j) pDOS calculations of NFM118 and MFM118.

shift and enhanced dispersion of the O 2p band. This reduces the charge-transfer energy between O 2p and Mn 3d orbitals and stabilizes the O 2p states. More significantly, the dispersed O 2p states represent more delocalized and stable electronic configurations that can reversibly accommodate holes during oxidation, preventing localized oxidative damage. This electronic structure reorganization achieved through Mg substitution reduces the energy barrier between Mn and O. This directly explains the key experimental observation from XANES (Fig. 5b): the anomalous reduction of Mn ($Mn^{4+} + e^- \rightarrow Mn^{3+}$) upon charging to 4.3 V. In this mechanism, the hole formed on the stabilized O 2p states is compensated by an electron from the Mn 3d orbital, and oxygen escape can be effectively suppressed. These calculations confirm that Mg substitution actively modulates the orbital energy level alignment by elevating and dispersing the O 2p band. This orbital-level engineering reduces the energy barrier for reversible electron transfer between Mn 3d and O 2p orbitals, thereby guiding the redox activity along a highly reversible anionic redox pathway and suppressing irreversible oxygen evolution.

## Conclusions

In summary, this work demonstrates a strategy for designing high-performance, low-cost, and Co/Ni-free cathodes by modulating charge compensation *via* orbital hybridization engineering. In $Na_{0.55}Mg_{0.1}Fe_{0.1}Mn_{0.8}O_2$, Mg substitution achieves superior performance not merely by structural stabilization but *via* active modulation of the local electronic structure. Specifically, the $Mg^{2+}$ substitution eliminates strong hybridization and elevates/improves the O 2p band, which lowers the energy barrier for charge transfer between Mn 3d and O 2p orbitals. As a result, the charge compensation proceeds *via* reversible electron transfer from $Mn^{4+}$ to stabilized O 2p states, effectively suppressing the Jahn–Teller effect, irreversible phase transitions, and oxygen release. This results in exceptional structural stability from the bulk to the interface, translating into high reversible capacity, remarkable rate capability, and long cycle life. This study establishes orbital hybridization engineering as a key principle for designing advanced SIB cathodes.

## Author contributions

Zhuozheng Hong: writing – original draft, formal analysis, investigation, data curation. Xin-Yu Zhang: writing – original draft, validation, conceptualization. Minwen Yang: writing – original draft, project administration, supervision, methodology. Yan-Fang Zhu: writing – review & editing, investigation, methodology. Diancheng Chen: writing – review & editing, supervision, conceptualization. Yan-Jiang Li: writing – review & editing, visualization, validation. Haojie Dong: writing – review & editing, software, investigation. YapingYan: funding acquisition, writing – review & editing. Yubin Niu: writing – review & editing, formal analysis, validation. Peng-Fei Wang: writing – review & editing, project administration. Yang Sun: funding

acquisition, writing – review & editing, project administration, conceptualization. Chao Wu: writing – original draft, writing – review & editing, methodology. Yao Xiao: writing – original draft, writing – review & editing, resources, funding acquisition, supervision.

## Conflicts of interest

The authors declare no conflict of interest.

## Data availability

Essential data are fully provided in the main text and supplementary information (SI). Supplementary information: experimental section, crystallography data and additional figures. See DOI: https://doi.org/10.1039/d6sc02906j.

## Acknowledgements

This work was financially supported by the National Natural Science Foundation of China (No. 52472240, 52402301, 22579131, and 22479166), the National Key R&D Program of China (2024YFA1211900), the Guangdong Innovative and Entrepreneurial Research Team Program (grant no. 2021ZT09L227), the Wenzhou Key Scientific and Technological Innovation Research Project (ZG2023053), the Open Fund Project of the State Key Laboratory of New Textile Materials and Advanced Processing, Wuhan Textile University (No. FZ2025008), and the Open Fund Project of the State Key Laboratory of Critical Metals Beneficiation, Metallurgy and Purification, Zhengzhou University (CM250205). We would like to thank Dr Yanan Zhao at the Analytical and Testing Center of Southwest University for her assistance with EPR analysis.

## References

1 J. Wang, Y.-F. Zhu, Y. Su, J.-X. Guo, S. Chen, H.-K. Liu, S.-X. Dou, S.-L. Chou and Y. Xiao, Routes to high-performance layered oxide cathodes for sodium-ion batteries, *Chem. Soc. Rev.*, 2024, **53**, 4230–4301.

2 X. Wang, Q. Zhang, C. Zhao, H. Li, B. Zhang, G. Zeng, Y. Tang, Z. Huang, I. Hwang, H. Zhang, S. Zhou, Y. Qiu, Y. Xiao, J. Cabana, C.-J. Sun, K. Amine, Y. Sun, Q. Wang, G.-L. Xu, L. Gu, Y. Qiao and S.-G. Sun, Achieving a high-performance sodium-ion pouch cell by regulating intergrowth structures in a layered oxide cathode with anionic redox, *Nat. Energy*, 2024, **9**, 184–196.

3 Y. Tang, Q. Zhang, W. Zuo, S. Zhou, G. Zeng, B. Zhang, H. Zhang, Z. Huang, L. Zheng, J. Xu, W. Yin, Y. Qiu, Y. Xiao, Q. Zhang, T. Zhao, H.-G. Liao, I. Hwang, C.-J. Sun, K. Amine, Q. Wang, Y. Sun, G.-L. Xu, L. Gu, Y. Qiao and S.-G. Sun, Sustainable layered cathode with suppressed phase transition for long-life sodium-ion batteries, *Nat. Sustain.*, 2024, **7**, 348–359.

4 Z.-Q. Li, Y.-F. Liu, H.-X. Liu, Y.-F. Zhu, J. Wang, M. Zhang, L. Qiu, X.-D. Guo, S.-L. Chou and Y. Xiao, Kinetically controlled synthesis of low-strain disordered micro–nano high voltage spinel cathodes with exposed {111} facets, *Chem. Sci.*, 2024, **15**, 11302–11310.

5 H.-Y. Hu, J.-Y. Li, Y.-F. Liu, Y.-F. Zhu, H.-W. Li, X.-B. Jia, Z.-C. Jian, H.-X. Liu, L.-Y. Kong, Z.-Q. Li, H.-H. Dong, M.-K. Zhang, L. Qiu, J.-Q. Wang, S.-Q. Chen, X.-W. Wu, X.-D. Guo and Y. Xiao, Developing an abnormal high-Na-content P2-type layered oxide cathode with near-zero-strain for high-performance sodium-ion batteries, *Chem. Sci.*, 2024, **15**, 5192–5200.

6 Z. Yu, C. Gan, A. S. Mijailovic, A. Stone, R. Hurt, C. L. Pernia, X. Xiao, C. Shi and B. W. Sheldon, Lithium Dendrite Deflection at Mixed Ionic–Electronic Conducting Interlayers in Solid Electrolytes, *Adv. Energy Mater.*, 2024, **15**, 2403179.

7 Z. Yu, C. Gan, S. Song, P. Guduru, K.-S. Kim and B. W. Sheldon, Dendrite suppression in garnet electrolytes via thermally induced compressive stress, *Joule*, 2026, **10**, 102232.

8 L. Qiu, M. Zhang, Y. Song, Z. Wu, Y. F. Zhu, J. Zhang, D. Wang, H. Y. Hu, H. W. Li, H. R. Liu, X. B. Jia, J. Peng, S. Chen, Z. Yang, Y. Xiao and X. Guo, Deciphering the degradation discrepancy in Ni-rich cathodes with a diverse proportion of [003] crystallographic textures, *Carbon Energy*, 2022, **5**, e298.

9 A. Yang, K. Yao, M. Schaller, E. Dashjav, H. Li, S. Zhao, Q. Zhang, M. Etter, X. Shen, H. Song, Q. Lu, R. Ye, I. Moudrakovski, Q. Pang, S. Indris, X. Wang, Q. Ma, F. Tietz, J. Chen and O. Guillon, Enhanced room-temperature $Na^+$ ionic conductivity in $Na_{4.92}Y_{0.92}Zr_{0.08}Si_4O_{12}$, *eScience*, 2023, **3**, 100175.

10 H. Li, Y. Wang, X. Zhao, J. Jin, Q. Shen, J. Li, Y. Liu, X. Qu, L. Jiao and Y. Liu, A Multielectron-Reaction and Low-Strain $Na_{3.5}Fe_{0.5}VCr_{0.5}(PO_4)_3$ Cathode for Na-Ion Batteries, *ACS Energy Lett.*, 2023, **8**, 3666–3675.

11 Z. Liu, J. Wu, J. Zeng, F. Li, C. Peng, D. Xue, M. Zhu and J. Liu, Co-Free Layered Oxide Cathode Material with Stable Anionic Redox Reaction for Sodium-Ion Batteries, *Adv. Energy Mater.*, 2023, **13**, 2301471.

12 A. Joshi, S. Chakrabarty, S. H. Akella, A. Saha, A. Mukherjee, B. Schmerling, M. Ejgenberg, R. Sharma and M. Noked, High-Entropy Co-Free O3-Type Layered Oxyfluoride: A Promising Air-Stable Cathode for Sodium-Ion Batteries, *Adv. Mater.*, 2023, **35**, 2304440.

13 Y. Wang, X. Zhao, J. Jin, Q. Shen, N. Zhang, X. Qu, Y. Liu and L. Jiao, Low-cost layered oxide cathode involving cationic and anionic redox with a complete solid-solution sodium-storage behavior, *Energy Storage Mater.*, 2022, **47**, 44–50.

14 G. Liu, W. Xu, J. Wu, Y. Li, L. Chen, S. Li, Q. Ren and J. Wang, Unlocking high-rate O3 layered oxide cathode for Na-ion batteries via ion migration path modulation, *J. Energy Chem.*, 2023, **83**, 53–61.

15 Z.-C. Jian, Y.-F. Liu, Y.-F. Zhu, J.-Y. Li, H.-Y. Hu, J. Wang, L.-Y. Kong, X.-B. Jia, H.-X. Liu, J.-X. Guo, M.-Y. Li, Y.-S. Xu, J.-F. Mao, S.-L. Zhang, Y. Su, S.-X. Dou, S.-L. Chou and Y. Xiao, Solid-state synthesis of low-cost and high-energy-density sodium layered-tunnel oxide cathodes: Dynamic structural evolution, $Na^+$/vacancy disordering, and

prominent moisture stability, *Nano Energy*, 2024, **125**, 109528.

16 Y. Li, Z.-Y. Li, K. Sun, Y.-T. Liu, D.-F. Chen, S.-B. Han, L.-F. He, M.-J. Li, X.-L. Liu and M.-M. Wu, Layered Co/Ni-free Mn-rich oxide P2-$Na_{2/3}Mn_{0.8}Fe_{0.1}Mg_{0.1}O_2$ as high-performance cathode material for sodium-ion batteries, *Ionics*, 2019, **26**, 735–743.

17 Z. Qiao, R. Ma, Y. Jia, H. Wu, L. Wang, A. Wang, S. Liu and J. Luo, A High-Entropy Strategy to Enhance the Structure and Electrochemical Performance of $NaNi_{1/3}Fe_{1/3}Mn_{1/3}O_2$ Cathodes, *ACS Appl. Energy Mater.*, 2025, **8**, 18021–18028.

18 H. Y. Hu, Y. F. Zhu, Y. Xiao, S. Li, J. Y. Li, Z. Q. Hao, J. H. Zhao and S. L. Chou, Strain Engineering by Local Chemistry Manipulation of Triphase Heterostructured Oxide Cathodes to Facilitate Phase Transitions for High-Performance Sodium-Ion Batteries, *Adv. Energy Mater.*, 2022, **12**, 2201511.

19 T. Chen, C. Wen, C. Wu, L. Qiu, Z. Wu, J. Li, Y. Zhu, H. Li, Q. Kong, Y. Song, F. Wan, M. Chen, I. Saadoune, B. Zhong, S. Dou, Y. Xiao and X. Guo, Manipulating the crystal plane angle within the primary particle arrangement for the radial ordered structure in a Ni-rich cathode, *Chem. Sci.*, 2023, **14**, 13924–13933.

20 K. Zhang, Z. Xu, G. Li, R. J. Luo, C. Ma, Y. Wang, Y. N. Zhou and Y. Xia, Regulating Phase Transition and Oxygen Redox to Achieve Stable High-Voltage O3-Type Cathode Materials for Sodium-Ion Batteries, *Adv. Energy Mater.*, 2023, **13**, 2302793.

21 Y. Zhang, B. Wu, J. Bi, X. Zhang, D. Mu, X. Y. Zhang, L. Zhang, Y. Xiao and F. Wu, Facilitating prelithiation of silicon carbon anode by localized high-concentration electrolyte for high-rate and long-cycle lithium storage, *Carbon Energy*, 2024, **6**, e480.

22 X. Wang, Z. Yang, D. Chen, B. Lu, Q. Zhang, Y. Hou, Z. Wu, Z. Ye, T. Li and J. Lu, Structural Regulation of P2-Type Layered Oxide with Anion/Cation Codoping Strategy for Sodium-Ion Batteries, *Adv. Funct. Mater.*, 2024, **35**, 2418322.

23 C. Wu, Y. Xu, J. Song, Y. Hou, S. Jiang, R. He, A. Wei, J. Tian and Q. Tan, Layered Hierarchical Modification Strategy in P2-Type Oxide Cathodes Enables High-Rate Capability and Long-Term Stability for Sodium-Ion Batteries, *ACS Appl. Mater. Interfaces*, 2025, **17**, 58203–58221.

24 C. Zhao, Z. Yao, Q. Wang, H. Li, J. Wang, M. Liu, S. Ganapathy, Y. Lu, J. Cabana, B. Li, X. Bai, A. Aspuru-Guzik, M. Wagemaker, L. Chen and Y. S. Hu, Revealing High Na-Content P2-Type Layered Oxides as Advanced Sodium-Ion Cathodes, *J. Am. Chem. Soc.*, 2020, **142**, 5742–5750.

25 X. Z. Wang, Y. Zuo, Y. Qin, X. Zhu, S. W. Xu, Y. J. Guo, T. Yan, L. Zhang, Z. Gao, L. Yu, M. Liu, Y. X. Yin, Y. Cheng, P. F. Wang and Y. G. Guo, Fast $Na^+$ Kinetics and Suppressed Voltage Hysteresis Enabled by a High-Entropy Strategy for Sodium Oxide Cathodes, *Adv. Mater.*, 2024, **36**, 2312300.

26 J. U. Choi, J. H. Jo, Y. J. Park, K. S. Lee and S. T. Myung, Mn-Rich P′2-$Na_{0.67}[Ni_{0.1}Fe_{0.1}Mn_{0.8}]O_2$ as High-Energy-Density and Long-Life Cathode Material for Sodium-Ion Batteries, *Adv. Energy Mater.*, 2020, **10**, 2001346.

27 B. Wang, X. Chen, X. Chen, Y. Wang, D. Qi, Y. Huang, X. Jiang, J.-H. Liu, P. Yan and Y. Xiao, High-performance $MnO_2$-based cathodes for aqueous zinc-ion batteries: Challenges, strategies, and perspectives, *eScience Energy*, 2025, **1**, 100008.

28 L. Sun, Z. Wu, M. Hou, Y. Ni, H. Sun, P. Jiao, H. Li, W. Zhang, L. Zhang, K. Zhang, F. Cheng and J. Chen, Unraveling and suppressing the voltage decay of high-capacity cathode materials for sodium-ion batteries, *Energy Environ. Sci.*, 2024, **17**, 210–218.

29 J. Feng, S. h. Luo, L. Qian, S. Yan, Q. Wang, X. Ji, Y. Zhang, X. Liu, P. Hou and F. Teng, Properties of the "Z"-Phase in Mn-Rich P2-$Na_{0.67}Ni_{0.1}Mn_{0.8}Fe_{0.1}O_2$ as Sodium-Ion-Battery Cathodes, *Small*, 2023, **19**, 2208005.

30 R. Liu, L. Yu, X. He, H. Liu, X. Ma, Z. Tao, G. Wan, N. Ahmad, B. Peng, L. Shi and G. Zhang, Constructing heterointerface of $Bi/Bi_2S_3$ with built-in electric field realizes superior sodium-ion storage capability, *eScience*, 2023, **3**, 100138.

31 H. Gao, J. Li, F. Zhang, C. Li, J. Xiao, X. Nie, G. Zhang, Y. Xiao, D. Zhang, X. Guo, Y. Wang, Y. M. Kang, G. Wang and H. Liu, Revealing the Potential and Challenges of High-Entropy Layered Cathodes for Sodium-Based Energy Storage, *Adv. Energy Mater.*, 2024, **14**, 2304529.

32 J. Zhang, Z. Yu, Y. Zhu, J. Cai, M. Wang, P. Gao, Y. Zhang, N. Zhang, D. Wang, Y. Shen and M. Wang, Configuration Design and Interface Reconstruction to Realize the Superior High-Rate Performance for Sodium Layered Oxide Cathodes, *Adv. Energy Mater.*, 2025, **15**, 2405951.

33 Y. He, Y. Huo, M. Xu and Y. Qi, Enhanced Anionic Redox Stability for Sodium Ion Battery Cathodes via Mg-Modified P2/O3 Biphasic Architecture, *Adv. Funct. Mater.*, 2025, **35**, 2509099.

34 A. Tang, R. Zhao, Y. Wu, C. Wan, Z. Li, X. Meng, K. Sun, R. Li, H. Zhang, D. Chen and X. Ju, Ligand-to-Metal Charge Transfer Motivated the Whole-Voltage-Range Anionic Redox in P2-Type Layered Oxide Cathodes, *Adv. Funct. Mater.*, 2024, **34**, 2402639.

35 Q. Zhou, Y. Li, S. Li, Z. Wang, Q. Li, X. Lu, Z. Qiu, C. Wu and Y. Bai, Ligand-Field Splitting Parameter Optimization Achieves Synergistic Enhancement of Transition Metal Redox Activity and Structural Stability in High-Voltage Sodium Layered Oxide Cathodes, *Adv. Funct. Mater.*, 2025, **35**, e09825.

36 A. Gao, X. Li, Q. Zhang, T. Lin, Y. Wang, Y. Chen, W. Lin, S. Wang, P. Ji, Z. Luo, J. Wang, Y. Guo and L. Gu, Dynamic Transition Metal Network via Orbital Population Design Stabilizes Lattice Oxygen Redox in Stoichiometric Layered Cathodes, *Adv. Mater.*, 2024, **37**, 2412673.

37 X. Rong, D. Xiao, Q. Li, Y. Niu, F. Ding, X. Hou, Q. Wang, J. Xu, C. Zhao, D. Zhou, R. Xiao, X. Yu, W. Yin, L. Gu, H. Li, X. Huang, L. Chen and Y.-S. Hu, Boosting reversible anionic redox reaction with Li/Cu dual honeycomb centers, *eScience*, 2023, **3**, 100159.

38 A. N. Singh, M. Islam, A. Meena, M. Faizan, D. Han, C. Bathula, A. Hajibabaei, R. Anand and K. W. Nam,

 

Unleashing the Potential of Sodium-Ion Batteries: Current State and Future Directions for Sustainable Energy Storage, *Adv. Funct. Mater.*, 2023, **33**, 2304617.

39 J. Liu, R. Liu, J. Lang, Y. Song, C. Wang, C. Wei, Y. Cui, Y. Xia and H. Li, The suppression effect of Mg doping on oxygen redox in Mn-based layered oxide cathodes for sodium-ion batteries, *Appl. Phys. Lett.*, 2025, **127**, 053901.

40 X. Han, X. Li, R. Chai, S. Wang, Y. Yuan and Y. Li, Trace $Mg^{2+}$ Doping Enhances Structural Stability of SingleCrystal Layered Oxides for Sodium-Ion Batteries, *Prog. Nat. Sci.:Mater. Int.*, 2025, **35**, 533–540.

41 Y. Ma, H. Zhang, L. Xie, W. Hua, Z. Huang, X. Sun, J. Luo, C. Shu, K. Yang and W. Tang, Substitution of magnesium towards stabilizing low-nickel layered oxides for high voltage and cost-effective sodium-ion batteries, *Sustainable Energy Fuels*, 2025, **9**, 981–990.

42 X. Zhang, W. Zuo, S. Liu, C. Zhao, Q. Li, Y. Gao, X. Liu, D. Xiao, I. Hwang, Y. Ren, C. J. Sun, Z. Chen, B. Wang, Y. Feng, W. Yang, G. L. Xu, K. Amine and H. Yu, High-Energy Earth-Abundant Cathodes with Enhanced Cationic/Anionic Redox for Sustainable and Long-Lasting Na-Ion Batteries, *Adv. Mater.*, 2024, **36**, 2310659.

43 X. Chen, G. Lin, P. Liu, Z. Sun, Y. Si, Q. Wang and L. Jiao, Synergetic enhancement of structural stability and kinetics of P′2-type layered cathode for sodium-ion batteries via cation–anion co-doping, *Energy Storage Mater.*, 2024, **67**, 103303.

44 Y. Hou, J. Jin, C. Huo, Y. Liu, S. Deng and J. Chen, New insights into the critical role of inactive element substitution in improving the rate performance of sodium oxide cathode material, *Energy Storage Mater.*, 2023, **56**, 87–95.

45 Y. Huo, H. Guo, Z. Hong, L. Xie, Y. He, W. Cao, M. Xu, Y. Xiao and Y. Qi, A Universal Voltage-Enhancement Strategy Based on Multifunctional Ligand-Mediated Modulation for Na-Layered Oxide Cathode, *Angew. Chem., Int. Ed.*, 2025, **64**, e202513023.

46 Y. J. Li, Y. F. Zhu, B. B. Chen, X. B. Jia, H. Xin, G. Z. Zhao, G. Zhu, S. X. Dou and Y. Xiao, Jahn-Teller Effect in Sodium Layered Oxide Cathodes: Inducement Mechanisms, Mitigation Strategies, and Rational Utilizations, *Adv. Funct. Mater.*, 2025, **35**, 2504096.

47 D. Yang, C. Liu, X. W. Gao, Z. Zhao, Q. Gu, Y. Long, Q. Lai, H. Chen, Z. Liu and W. B. Luo, Constructing Mechanical–Chemical Stability via Multiphase Riveting and Interface Optimization Toward Layer-structured Oxide Cathode Material, *Angew. Chem., Int. Ed.*, 2025, **64**, e202500939.

48 X.-B. Jia, Q.-Q. Peng, Y.-F. Liu, D.-C. Chen, J. Wang, J.-Y. Li, Y.-F. Zhu, N.-H. Xu, L.-Y. Kong, H.-X. Liu, G.-Y. Zhang, Z.-C. Jian, C. Cheng, H.-H. Dong, L. Zhang, Y. Sun, S.-Q. Chen, X.-D. Guo, S. Dou and Y. Xiao, Design principles of practical industrial-scale layered oxide cathodes with air/water stability for sustainable sodium-ion batteries, *Nat. Commun.*, 2025, **16**, 10477.

49 Y. Li, K. A. Mazzio, N. Yaqoob, Y. Sun, A. I. Freytag, D. Wong, C. Schulz, V. Baran, A. S. J. Mendez, G. Schuck, M. Zając, P. Kaghazchi and P. Adelhelm, Competing Mechanisms Determine Oxygen Redox in Doped Ni–Mn Based Layered Oxides for Na-Ion Batteries, *Adv. Mater.*, 2024, **36**, 2309842.

50 X. Ding, W. Yuan, J. Lin, H. Li, X. Yang, L. Liu, Y. Xiao, F. Chen and L. Han, In-situ surface coating and subsurface gradient doping contrives P2-$Na_{0.67}Ni_{0.33}Mn_{0.67}O_2$ single crystal with highly stable interface and structure, *Nano Res. Energy*, 2025, **4**, e9120203.

51 C. Guo, X. Y. Fan, M. Liu, S. W. Xu, G. X. Wei, Z. B. Chen, Z. K. Guan, Y. Xiao, H. Xin and P. F. Wang, Amorphous Protective Layers to Reshape Inorganic-Rich Interphases for High-Voltage Sodium-Ion Batteries, *Carbon Energy*, 2025, e70037, DOI: 10.1002/cey2.70037.

52 J. Sun, H. Yang, J. Shen, H. Qi, M. Sun, Y. Lou, Y. Yao, X. Rui, Y. Shao, X. Wu and Y. Yu, Incorporating a lithium-deficient layer and interfacial-confined catalysis enables the reversible redox of surface oxygen species in lithium-rich manganese-based oxides, *Energy Environ. Sci.*, 2025, **18**, 4335–4347.

53 Y. Niu, Z. Hu, H. Mao, L. Zhou, L. Wang, X. Lou, B. Zhang, D. Xiao, Y. Yang, F. Ding, X. Rong, J. Xu, W. Yin, N. Zhang, Z. Li, Y. Lu, B. Hu, J. Lu, J. Li and Y.-S. Hu, A "seat-squatting" strategy via lithium substitution to suppress Fe-migration in Na layered oxide cathodes, *Energy Environ. Sci.*, 2024, **17**, 7958–7968.

54 H. Liu, W. Hua, S. Kunz, M. Bianchini, H. Li, J. Peng, J. Lin, O. Dolotko, T. Bergfeldt, K. Wang, C. Kübel, P. Nagel, S. Schuppler, M. Merz, B. Ying, K. Kleiner, S. Mangold, D. Wong, V. Baran, M. Knapp, H. Ehrenberg and S. Indris, Tailoring superstructure units for improved oxygen redox activity in Li-rich layered oxide battery's positive electrodes, *Nat. Commun.*, 2024, **15**, 9981.

55 Z.-C. Jian, W. Shi, Y. Liu, X. Li, J. Li, Y.-F. Zhu, X. Zhu, Y. Li, P. Tan, P.-F. Wang, S. Chen, S. Zhang, J. Mao, G. Zhou, X. Guo, J. Wang, S.-X. Dou and Y. Xiao, Accelerating lattice oxygen kinetics of layered oxide cathodes via active facet modulation and robust mechanochemical interface construction for high-energy-density sodium-ion batteries, *Energy Environ. Sci.*, 2025, **18**, 7995–8008.

56 H. Y. Hu, M. Yang, D. Chen, N. H. Xu, J. Y. Li, Y. F. Zhu, Y. B. Wu, H. H. Dong, J. Wang, C. Yao, Y. Yan, S. Chen, N. Wang, W. K. Pang, Y. Sun, J. Z. Wang and Y. Xiao, Spatially Selective Substitution for Structural Stabilization of Sodium Layered Oxide Cathodes, *Angew. Chem., Int. Ed.*, 2025, **65**, e19108.

57 L. Ran, B. Shen, L. Yue, H. Hu, Y. Xiang, Z. Jiang, Z. Li, Y. Duan, Y. Zhao, Y. Zheng, M. Xu, Y. Xiao and Y. Niu, Accelerating Electrochemical Kinetics in $Na_4Fe_3(PO_4)_2P_2O_7$ Cathodes Through Oxygen Vacancy Modulation for Wide-Temperature Ah-Level Sodium-Ion Batteries, *Angew. Chem., Int. Ed.*, 2026, **65**, e25531.

58 X. B. Jia, J. Wang, Y. F. Liu, Y. F. Zhu, J. Y. Li, Y. J. Li, S. L. Chou and Y. Xiao, Facilitating Layered Oxide Cathodes Based on Orbital Hybridization for Sodium-Ion

Batteries: Marvelous Air Stability, Controllable High Voltage, and Anion Redox Chemistry, *Adv. Mater.*, 2024, **36**, 2307938.

59 S. Chakrabarti and A. K. Thakur, Density functional theory study of novel high voltage cathode materials $LiMSbO_4$ (M=Ni/Co/Fe/Mn) for Li ion battery applications, *Mater. Chem. Phys.*, 2025, **338**, 130655.

60 Y. Wu, Y. Dang, Z. Xiao, R. Zheng, Z. Song, Q. Wang, J. Mao, D. Wang, Y. Liu and Z. Wang, Mg anti-site occupation suppresses Fe migration in O3-type $NaNi_{1/3}Fe_{1/3}Mn_{1/3}O_2$ cathodes toward high-performance sodium-ion batteries, *Energy Storage Mater.*, 2025, **83**, 104736.